Title

Crystal growth, characterization and physical properties of PrNiSb3, NdNiSb3 and SmNiSb3

Journal

Journal of Solid State Chemistry, 177(11)

ISSN
0022-4596

Authors

Thomas, Evan L
Macaluso, Robin T
Lee, Han-Oh
et al.

Publication Date

2004-11-01

DOI
10.1016/j.jssc.2004.08.014

Available online at www.sciencedirect.com

SCIENCE DIRECT®

ELSEVIER

Journal of Solid State Chemistry 177 (2004) 4228–4236

JOURNAL OF SOLID STATE CHEMISTRY

www.elsevier.com/locate/jssc

Crystal growth, characterization and physical properties of $PrNiSb_3$, $NdNiSb_3$ and $SmNiSb_3$

Evan L. Thomas[a], Robin T. Macaluso[a], Han-Oh Lee[b], Zachary Fisk[b], Julia Y. Chan[a,*]

[a]Department of Chemistry, Louisiana State University, Room 232 Choppin Hall, Baton Rouge, LA 70803, USA
[b]Department of Physics, University of California, One Shields Ave., Davis, CA 95616, USA

Received 21 June 2004; received in revised form 6 August 2004; accepted 8 August 2004

Abstract

The crystal structures of three new intermetallic ternary compounds in the $LnNiSb_3$ (Ln = Pr, Nd and Sm) family have been characterized by single crystal X-ray diffraction. $PrNiSb_3$, $NdNiSb_3$ and $SmNiSb_3$ all crystallize in an orthorhombic space group, *Pbcm* (No. 57), $Z = 12$, with $a = 12.5700(2)$ Å, $b = 6.2010(4)$ Å, $c = 18.670(6)$ Å, and $V = 1431.64(11)$ Å^3; $a = 12.5090(2)$ Å, $b = 6.1940(3)$ Å, $c = 18.3350(6)$ Å, and $V = 1420.61(9)$ Å^3; and $a = 12.3900(1)$ Å, $b = 6.1760(3)$ Å, $c = 18.2650(6)$ Å, and $V = 1397.65(8)$ Å^3, for Ln = Pr, Nd and Sm, respectively. These compounds consist of rare-earth atoms located above and below layers of nearly square, buckled Sb nets, along with layers of highly distorted edge- and face-sharing $NiSb_6$ octahedra. Resistivity data indicate metallic behavior for all three compounds. Magnetization measurements show antiferromagnetic behavior with $T_N = 4.5$ K ($PrNiSb_3$), 4.6 K ($NdNiSb_3$), and 2.9 K ($SmNiSb_3$). Effective moments of 3.62 μ_B, 3.90 μ_B and 0.80 μ_B are found for $PrNiSb_3$, $NdNiSb_3$ and $SmNiSb_3$, respectively, and are consistent with Pr^{3+} (f^2), Nd^{3+} (f^3), and Sm^{3+} (f^4).

Keywords: $PrNiSb_3$; Square net; Resistivity; Rare-earth antimonides; Single crystals; $CeNiSb_3$; Crystal growth; $LnNiSb_3$; X-ray diffraction

---

1. Introduction

Ternary rare-earth (lanthanide) transition metal antimonides, Ln–T–Sb, display a variety of interesting physical properties [1]. The Zintl phase $Eu_{14}MnSb_{11}$, exhibits colossal magnetoresistance (up to −36%) and shows a ferromagnetic transition at 92 K [2]. Recently, the first Pr-based heavy-fermion compound, $PrOs_4Sb_{12}$, was found to be superconducting below $T_C = 1.85$ K [3]. In the Ln–Ni–Sb system, $CeNiSb_2$ exhibits a ferromagnetic ground state below 6 K and shows large magnetic anisotropy [4].

Another interesting class of Sb-containing compounds is $LaTSb_3$ (T = V, Cr) [5,6]. The V and Cr analogs of $LaTSb_3$ are isostructural and consist of planes of nearly square Sb nets, with Ln atoms positioned both above and below these Sb net planes. Also included are layers of TSb_6 octahedra which are face sharing along the c-axis and edge sharing along the b-axis [7]. The $LnVSb_3$ (Ln = La–Nd, Sm) phases show no magnetic ordering for the transition metal and therefore no 3d moment is present [8]. However, the Cr analog shows two magnetic transitions—one for the ordering of Cr at high temperatures (T_{Cr}~132 K) [6,9,10] and a second for the coupled Ln–Cr ordering found at low temperatures ($T_{Ln\text{–}Cr}$~10 K) [6,8–13]. $NdCrSb_3$ shows negative magnetoresistance up to −13% at 5 K with an applied field of 4 T [13].

Closely related to the structure of $LaCrSb_3$ is $CeNiSb_3$, for which the synthesis and structure have been recently reported [14]. The structure of $CeNiSb_3$ also consists of distorted, nearly square Sb nets capped by Ce atoms, and Ni octahedra layers. However, the

---

*Corresponding author. Fax: +1-225-578-3458.
E-mail address: jchan@lsu.edu (J.Y. Chan).

0022-4596/$ - see front matter
doi:10.1016/j.jssc.2004.08.014

$NiSb_6$ octahedra are face- and edge sharing along the *c*-axis. Resistivity measurements for $CeNiSb_3$ suggest Kondo lattice behavior [14].

We report here the synthesis, structure, and measurements of electrical and magnetic properties of three new phases, *Ln*$NiSb_3$ (*Ln* = Pr, Nd and Sm). The systematic substitution of the lanthanide atom allows for the opportunity to investigate the effects of the structure, particularly of the distorted Sb sheets and $NiSb_6$ octahedra, on the physical properties of these antimonides.

2. Experimental

2.1. Synthesis

Single crystals of *Ln*$NiSb_3$ (*Ln* = Pr, Nd and Sm) were prepared with excess Sb. These phases were synthesized by placing ingots of Pr (99.9% purity, Alfa Aesar), Nd (99.9% purity, Alfa Aesar), or Sm (99.9% purity, Alfa Aesar), along with Ni powder (99.999% purity, Alfa Aesar), and Sb shot (99.9999% purity, Alfa Aesar), into alumina crucibles in a 1:2:20 (*Ln*:Ni:Sb) molar ratio. Each crucible was sealed into an evacuated silica tube. The samples were heated to 1150 °C and cooled at a rate of $5\,°C\,h^{-1}$ to 670 °C, at which point, excess flux was removed by centrifugation. Once the samples were cooled to room temperature, the metallic, plate-shaped crystals with dimensions up to $1 \times 2 \times 2.5\,mm^3$, were mechanically extracted. The crystals possessed clean surfaces with no evidence of flux contamination and appeared to be moisture sensitive after a week of exposure to air (apparent by the grayish color change).

2.2. Physical property measurements

Magnetic moments were measured using a Quantum Design SQUID magnetometer. The temperature-dependent susceptibility data were taken with the applied field of 1000 G up to room temperature after being cooled to 1.8 K under zero magnetic field. Magnetic field-dependent magnetization data were also checked from zero field to 5.5 T at 2 K. The resistivity data have been measured using a standard four-probe method down to 0.35 K with Quantum Design Physical Property Measurement System at ambient pressure.

2.3. Single crystal X-ray diffraction

Plate-shaped crystals with dimensions of approximately $0.040 \times 0.100 \times 0.080\,mm^3$ ($PrNiSb_3$), $0.050 \times 0.025 \times 0.125\,mm^3$ ($NdNiSb_3$), and $0.075 \times 0.050 \times 0.100\,mm^3$ ($SmNiSb_3$) were mounted onto a glass fiber of a goniometer and placed on a Nonius Kappa CCD X-ray diffractometer (Mo$K\alpha$ = 0.71073 Å). Data were collected at 298 K. Data collection parameters and crystallographic data are provided in Table 1. The lattice parameters were determined from images taken

Table 1
Structural refinement data for $PrNiSb_3$, $NdNiSb_3$ and $SmNiSb_3$

Formula	$PrNiSb_3$	$NdNiSb_3$	$SmNiSb_3$
Space group	*Pbcm*	*Pbcm*	*Pbcm*
a (Å)	12.5700(2)	12.5090(2)	12.3900(1)
b (Å)	6.2010(4)	6.1940(3)	6.1760(3)
c (Å)	18.3670(6)	18.3350(6)	18.2650(6)
V (Å^3)	1431.60(10)	1420.61(9)	1397.65(8)
Crystal dimensions (mm^3)	$0.040 \times 0.100 \times 0.080$	$0.050 \times 0.025 \times 0.125$	$0.075 \times 0.050 \times 0.100$
Z	12	12	12
Temperature (°C)	25	25	26
Crystal density (g cm^{-3})	7.862	7.920	8.188
θ range (deg)	2.75–30.03	2.75–30.04	2.77–30.01
μ (mm^{-1})	30.45	31.36	33.34
Collected reflections	13832	15058	15097
Unique reflections	2155	2141	2105
R_{int}	0.0585	0.0459	0.0322
h	$-17 \leqslant h \leqslant 17$	$-17 \leqslant h \leqslant 17$	$-17 \leqslant h \leqslant 17$
k	$-8 \leqslant k \leqslant 8$	$-8 \leqslant k \leqslant 8$	$-8 \leqslant k \leqslant 8$
l	$-25 \leqslant l \leqslant 25$	$-25 \leqslant l \leqslant 25$	$-25 \leqslant l \leqslant 25$
$\Delta\rho_{max}$ (e Å^{-3})	3.831	4.119	2.954
$\Delta\rho_{min}$ (e Å^{-3})	−2.698	−2.467	−3.014
Extinction coefficient	0.00041(3)	0.00041(3)	0.00020(2)
$R(F)$ for $F_o^2 > 2\sigma(F_o^2)$ [a]	0.0432	0.0406	0.0360
$R_w(F_o^2)$ [b]	0.0704	0.0588	0.0486

[a] $R(F) = \sum ||F_o| - |F_c|| / \sum |F_o|$.
[b] $R_w(F_o^2) = \sum [w(F_o^2 - F_c^2)] / \sum [w(F_o^2)^2]^{1/2}$.

from a scan in 10 °φ. The structures were solved using the structure of CeNiSb$_3$ [14] as an initial structural model and were refined using SHELXL97 [15]. After the refinement of atomic positions, the data were corrected for absorption and displacement parameters were refined as anisotropic. Extinction and weighting schemes were also applied to the refinement. The $R[F^2 > 2\sigma(F^2)]$ was 4.32%, 4.06% and 3.60%, with largest features in the difference map of 3.831/−2.698 e Å^{-3}, 4.119/−2.467 e Å^{-3} and 2.954/−3.014 e Å^{-3} for *Ln* = Pr, Nd and Sm, respectively. Atomic coordinates and anisotropic displacement parameters are provided in Table 2. Table 3 provides selected interatomic distances for CeNiSb$_3$ [14], PrNiSb$_3$, NdNiSb$_3$ and SmNiSb$_3$ for comparison. Detailed data collection parameters and crystallographic data are provided as Supporting Information.

3. Results and discussion

3.1. Structure

*Ln*NiSb$_3$ (*Ln* = Pr, Nd and Sm) crystallize in the CeNiSb$_3$ structure type [14]. The lattice parameters are provided in Table 1 and the structure of PrNiSb$_3$ is shown in Fig. 1. The structure of *Ln*NiSb$_3$ (*Ln* = Ce–Nd and Sm) has been described as being built up of *Ln* atoms between layers of highly distorted, Ni-centered octahedra, and layers of buckled, nearly square Sb nets [14].

The distorted Sb nets found in *Ln*NiSb$_3$ (*Ln* = Pr, Nd, Sm) are composed of 4-coordinate Sb1 and Sb3 atoms. For *Ln* = Pr, the Sb1–Sb1 and Sb3–Sb3 bonds with distances of 3.1018(2) Å regularly repeat along the *b*-direction, but Sb1–Sb3 and Sb1–Sb1 bonds with

Table 2
Atomic positions, site symmetry and U_{eq} values for *Ln*NiSb$_3$ (*Ln* = Pr, Nd and Sm)

Atom	Wyckoff site	*x*	*y*	*z*	U_{eq} (Å^2)[a]
PrNiSb$_3$					
Pr1	4*d*	0.305851(6)	0.55725(1)	$\frac{3}{4}$	0.0103(2)
Pr2	8*e*	0.299273(5)	0.026176(9)	0.583435(3)	0.0102(2)
Ni1	4*c*	0.10296(2)	$\frac{3}{4}$	$\frac{1}{2}$	0.0116(4)
Ni2	8*e*	0.09879(1)	0.32819(2)	0.675884(7)	0.0139(3)
Sb1	8*e*	0.496457(5)	0.29307(1)	0.665923(4)	0.0112(2)
Sb2	4*d*	0.221053(8)	0.05208(2)	$\frac{3}{4}$	0.0113(2)
Sb3	4*c*	0.503933(8)	$\frac{1}{4}$	$\frac{1}{2}$	0.0123(2)
Sb4	8*e*	0.225541(6)	0.52539(1)	0.584212(4)	0.0107(2)
Sb5	8*e*	0.974097(6)	0.54324(1)	0.586646(4)	0.0115(1)
Sb6	4*c*	0.058303(8)	0.68819(2)	$\frac{3}{4}$	0.0112(2)
NdNiSb$_3$					
Nd1	4*d*	0.306096(5)	0.55828(1)	$\frac{3}{4}$	0.0113(2)
Nd2	8*e*	0.299445(4)	0.026593(8)	0.583481(3)	0.0116(2)
Ni1	4*c*	0.10350(1)	$\frac{3}{4}$	$\frac{1}{2}$	0.0123(2)
Ni2	8*e*	0.09982(1)	0.32803(2)	0.675967(7)	0.0153(3)
Sb1	8*e*	0.496253(5)	0.29405(1)	0.665935(3)	0.0123(2)
Sb2	4*d*	0.222689(7)	0.05194(2)	$\frac{3}{4}$	0.0120(2)
Sb3	4*c*	0.504041(7)	$\frac{1}{4}$	$\frac{1}{2}$	0.0129(2)
Sb4	8*e*	0.227101(6)	0.52537(1)	0.584209(3)	0.0117(2)
Sb5	8*e*	0.973967(5)	0.54317(1)	0.586658(3)	0.0123(2)
Sb6	4*c*	0.058583(7)	0.68871(1)	$\frac{3}{4}$	0.0126(2)
SmNiSb$_3$					
Sm1	4*d*	0.306545(5)	0.56010(1)	$\frac{3}{4}$	0.0100(2)
Sm2	8*e*	0.299812(4)	0.027112(7)	0.583446(2)	0.0100(2)
Ni1	4*c*	0.10494(1)	$\frac{3}{4}$	$\frac{1}{2}$	0.0110(3)
Ni2	8*e*	0.10111(1)	0.32822(2)	0.676185(7)	0.0136(3)
Sb1	8*e*	0.496085(4)	0.294081(9)	0.666029(3)	0.0106(2)
Sb2	4*d*	0.225516(7)	0.05171(1)	$\frac{3}{4}$	0.0107(2)
Sb3	4*c*	0.504092(6)	$\frac{1}{4}$	$\frac{1}{2}$	0.0113(2)
Sb4	8*e*	0.229836(5)	0.525680(9)	0.584271(3)	0.0101(1)
Sb5	8*e*	0.973794(5)	0.543529(9)	0.586736(3)	0.0110(2)
Sb6	4*c*	0.059220(6)	0.68905(1)	$\frac{3}{4}$	0.0110(2)

[a] U_{eq} is defined as one-third of the trace of the orthogonalized U_{ij} tensor.

Table 3
Selected interatomic distances (Å) in LnNiSb$_3$ (Ln = Ce–Nd and Sm)

	CeNiSb$_3$ [14]	PrNiSb$_3$	NdNiSb$_3$	SmNiSb$_3$
Within Sb square sheets				
Sb1–Sb1 (×2)	3.1031(2)	3.1018(2)	3.0984(2)	3.0895(2)
Sb1–Sb1	3.0880(6)	3.089(1)	3.083(1)	3.067(1)
Sb1–Sb3	3.0616(3)	3.0606(7)	3.0562(6)	3.0468(6)
Sb3–Sb3 (×2)	3.1035(2)	3.1021(2)	3.0986(2)	3.0897(2)
Sb2–Sb6	3.0395(6)	3.046(1)	3.046(1)	3.043(1)
Sb4–Sb5	3.1568(5)	3.163(1)	3.1687(9)	3.1746(9)
Sb5–Sb5 (×2)	3.1714(2)	3.1682(4)	3.1647(3)	3.1555(3)
Sb5–Sb5	3.2929(6)	3.293(1)	3.288(1)	3.279(1)
Sb5–Sb6	3.3116(4)	3.3061(9)	3.3019(7)	3.2894(7)
Sb6–Sb2	3.0395(6)	3.046(1)	3.046(1)	3.043(1)
Sb6–Sb5 (×2)	3.3116(4)	3.061(9)	3.3018(7)	3.2894(7)
Ln1–Sb4 (×2)	3.2225(3)	3.2141(8)	3.2028(6)	3.1798(6)
Ln1–Sb6	3.2262(6)	3.216(1)	3.200(1)	3.166(1)
Ln1–Sb1 (×2)	3.2838(5)	3.271(1)	3.2590(8)	3.2305(8)
Ln1–Sb1 (×2)	3.2994(4)	3.288(1)	3.2730(8)	3.2478(8)
Ln1–Sb2	3.2629(6)	3.248(1)	3.231(1)	3.198(1)
Ln1–Sb2	3.3112(6)	3.309(1)	3.305(1)	3.296(1)
Ln1–Ni2 (×2)	3.2793(7)	3.263(2)	3.246(1)	3.217(1)
Ln2–Sb2	3.2260(3)	3.2174(7)	3.2044(6)	3.1820(5)
Ln2–Sb4	3.2400(4)	3.2315(9)	3.2193(8)	3.1989(7)
Ln2–Sb4	3.2408(4)	3.2315(9)	3.2211(8)	3.2003(7)
Ln2–Sb4	3.2501(4)	3.2408(9)	3.2338(8)	3.2159(7)
Ln2–Sb3	3.3137(4)	3.300(1)	3.2875(8)	3.2594(8)
Ln2–Sb1	3.3256(4)	3.3132(9)	3.3002(8)	3.2750(7)
Ln2–Sb1	3.3550(4)	3.3433(9)	3.3303(8)	3.3054(7)
Ln2–Sb3	3.3864(4)	3.3765(9)	3.3646(8)	3.3399(7)
Ln2–Sb5	3.4509(4)	3.4384(9)	3.4221(8)	3.3920(7)
Ln2–Ni1	3.3921(7)	3.372(2)	3.549(1)	3.329(1)

distances of 3.0606(7) and 3.0885(13) Å alternate along the c-direction. Sb–Sb interatomic distances for Ln = Ce, Nd, and Sm are shown in Table 3 and show similar distortions as seen for Ln = Pr. As Ln progresses from Ce to Sm, the Sb–Sb interatomic distances decrease. Perfectly square sheets have been found for the LnT_xSb$_2$ (T = Mn, Fe, Co, Ni, Cu, Zn, Pt, Pd, Cd, Ag, Au) compounds, where x is usually less than or equal to 1 [16–23]. The Sb–Sb–Sb angles in LnNiSb$_3$ (Ln = Ce–Nd, Sm) deviate from 90°, further indicating distorted Sb nearly square nets. Distorted Sb nets have also been found in LnCrSb$_3$ [7] and LnIn$_{1-x}$Sb$_2$ [24]. Substituting smaller lanthanide atoms bears only a slight influence on the Sb–Sb distances and Sb–Sb–Sb angles in the square nets of LnNiSb$_3$ (Ln = Ce–Nd, Sm).

The Ln (Pr, Nd, Sm) atoms are located above and below the Sb square net in a checkered fashion. Consequently, one can view the Ln layer as being interleaved between the Ni octahedra and Sb square nets [14]. The local monocapped-square antiprismatic Ln environment is shown as dashed lines in Fig. 1. This geometry is similar to the rare-earth capped antimony nets seen in LnSb$_2$ [25], CeNiSb$_2$ [26], and LnCrSb$_3$ [7]. In contrast to LnCrSb$_3$, however, the LnNiSb$_3$ phases contain two crystallographically inequivalent sites, Ln1 (4d) and Ln2 (8e), whereas the Ln atom in LnCrSb$_3$ occupies only one site. In LnNiSb$_3$, Ln1 is coordinated to four Sb1 atoms in the square net to form the base of the square antiprism and to four Sb atoms (two Sb2 and two Sb4) in the NiSb$_6$ layer to form a larger distorted square twisted by 45° relative to the basal square. Sb6, which is also in the NiSb$_6$ octahedra layer, caps the Ln1 square antiprism. Likewise, the Ln2 atom forms a monocapped square antiprism with four Sb atoms (two Sb1 and two Sb3) as the base, four Sb atoms (one Sb2 and three Sb4) as the opposing square, and an Sb5 atom as the cap. The distances between the Ln1 atom and the Sb1 square net atoms range from 3.2838(5)–3.2994(4) Å for Ce1 [14], 3.2708(10)–3.2877(10) Å for Pr1, 3.2591(9)–3.2730(8) Å for Nd1, and 3.2306(8)–3.2478(8) Å for Sm1; and the distances between Ln2 and Sb1 and Sb3 in the square net range from 3.3256(4)–3.3550(4) Å and 3.3864(4) Å for Ce2 [14], 3.3132(9)–3.3433(9) Å and 3.3721(15) Å for Pr2, 3.3002(8)–3.3303(8) Å and 3.3646(8) Å for Nd2, and 3.2750(7)–3.3054(7) Å and 3.3400(7) Å for Sm2. For

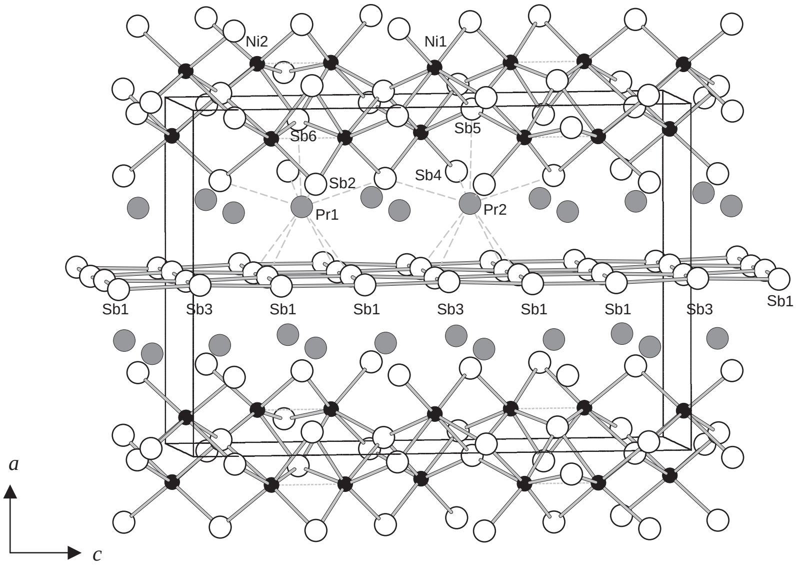

Fig. 1. The crystal structure of $PrNiSb_3$ viewed down the *b*-axis with the unit cell shown as a solid line. The shaded circles are Pr atoms, the solid circles are Ni atoms and the open circles are Sb atoms. The mono-capped square antiprism environments of the Pr1 and Pr2 atoms are shown as dashed lines.

comparison, the corresponding La–Sb3 distances in $LaCrSb_3$ (as LnCrSb$_3$ contains only Sb3 atoms in its square nets) range from 3.347(2)–3.355(2) Å [5].

The *Ln*–Sb interatomic distances and thus, the lattice parameters, decrease with ionic radii, as expected due to lanthanide contraction. As *Ln* progresses from Ce to Sm in LnNiSb$_3$, *a* decreases by ~2% and both the *b*- and *c*-parameters decrease by ~1%. The contraction of the *a*-parameter may induce bond strain between the *Ln* and Sb atoms and further distort the Ni octahedra, rendering the latter lanthanide analogs (Ln = Gd–Tm) unstable. Crystal growth of other analogs (Gd–Tm) were attempted; however, we obtained crystals of LnNiSb$_2$ for Gd–Er. When Ln = Tm, TmSb was the primary phase present. Similar results were found for the LnCrSb$_3$ (Ln = La–Nd, Sm, Gd–Dy) compounds, although a different synthetic route was employed for the synthesis of Ln = (Gd–Dy). Hence, it may be possible to prepare LnNiSb$_3$ (Ln = late lanthanides) with a different synthetic route.

In LnNiSb$_3$, there are Ni1 and Ni2 octahedra which run along the *b*-direction. These octahedra are edge sharing in the *b*-direction whereas they are face sharing with every third octahedron sharing edges in the *c*-direction. Table 4 provides the bond distances and angles for the Ni1 and Ni2 octahedra in LnNiSb$_3$ (Ln = Ce–Nd, Sm). The distances between Ni and Sb also contract with increasing *Ln* size, and are all in good agreement with the Ni–Sb distances of 2.6082 Å found in NiSb [27].

For the Ni1 octahedra, the largest degree of distortion is found for the "axial" Sb5′–Ni1–Sb5′ angle. These angles are expected to be 180°, but are actually observed to be 136.73(5)°, 136.32(8)°, 136.24(7)°, and 135.89(7)° for Ln = Ce [14], Pr, Nd, and Sm, respectively. These bond angles may constitute an enormous amount of angle tension and thus affect the stability of the latter lanthanide elements. The "equatorial" Sb4–Ni1–Sb4 angles (expected to be 90°) are found to be 107.02(3)°, 106.97(7)°, 106.71(6)°, and 106.46(6)° for Ln = Ce [14], Pr, Nd, and Sm, respectively. Consequently, the adjacent Sb5–Ni1–Sb5 angles are more acute (~75°). This pattern is seen in the Ni2 octahedra as well (see Table 4). The angles of Ni octahedra and Sb square nets of $SmNiSb_3$ are the most distorted. The Ni2–Ni2 distances are 2.7214(12) Å for Ce [14], 2.723(3) Å for Pr, 2.715(2) Å for Nd, and 2.696(2) Å for Sm, similar to the average Ni–Ni distance of 2.5675 Å found in NiSb [27].

3.2. Physical properties

Fig. 2 (a–c) shows the temperature-dependent susceptibility under applied magnetic field of 1000 G along the crystalline *bc*1- and *bc*2- planes and the *a*-axis. Cusps in the data indicate antiferromagnetic transitions in these systems and the corresponding Néel temperature is around 4.5, 4.6, and 2.9 K for $PrNiSb_3$, $NdNiSb_3$, and $SmNiSb_3$, respectively. The anisotropy in the susceptibility data is more obvious from the applied field along the crystalline *a*-axis than the field in the *bc*-plane. The inverse susceptibilities, shown in Fig. 2 insets, follow linear dependencies with temperature, suggesting Curie–Weiss behavior above the transition temperatures. Anisotropies at high temperature are small and the averaged effective moments from the high-temperature

Table 4
Selected bond distances (Å) and angles (deg) in Ni1 and Ni2 octahedra

	$CeNiSb_3$ [14]	$PrNiSb_3$	$NdNiSb_3$	$SmNiSb_3$
Bond				
Ni2–Ni2	2.721(1)	2.723(3)	2.715(2)	2.696(2)
Ni1–Sb4 (× 2)	2.5899(6)	2.590(1)	2.590(1)	2.585(1)
Ni1–Sb5 (× 2)	2.6049(6)	2.608(1)	2.606(1)	2.603(1)
Ni1–Sb5′ (× 2)	2.5973(4)	2.603(1)	2.6002(9)	2.5976(8)
Ni2–Sb2	2.6708(7)	2.673(2)	2.670(2)	2.666(1)
Ni2–Sb4	2.6186(7)	2.621(2)	2.619(1)	2.617(1)
Ni2–Sb5′	2.5778(7)	2.578(2)	2.578(1)	2.573(1)
Ni2–Sb5	2.6301(7)	2.631(2)	2.634(1)	2.632(1)
Ni2–Sb6	2.5498(7)	2.581(2)	2.552(1)	2.550(1)
Ni2–Sb6′	2.6624(7)	2.664(2)	2.665(2)	2.656(1)
Angle				
Sb4–Ni1–Sb4	107.02(3)	106.97(7)	106.71(6)	106.46(6)
Sb4–Ni1–Sb5	74.85(1)	74.77(2)	75.15(2)	75.45(2)
Sb4–Ni1–Sb5′	103.25(1)	103.41(2)	103.49(2)	103.63(2)
Sb5′–Ni1–Sb5′	136.89(4)	136.32(8)	136.24(7)	135.89(7)

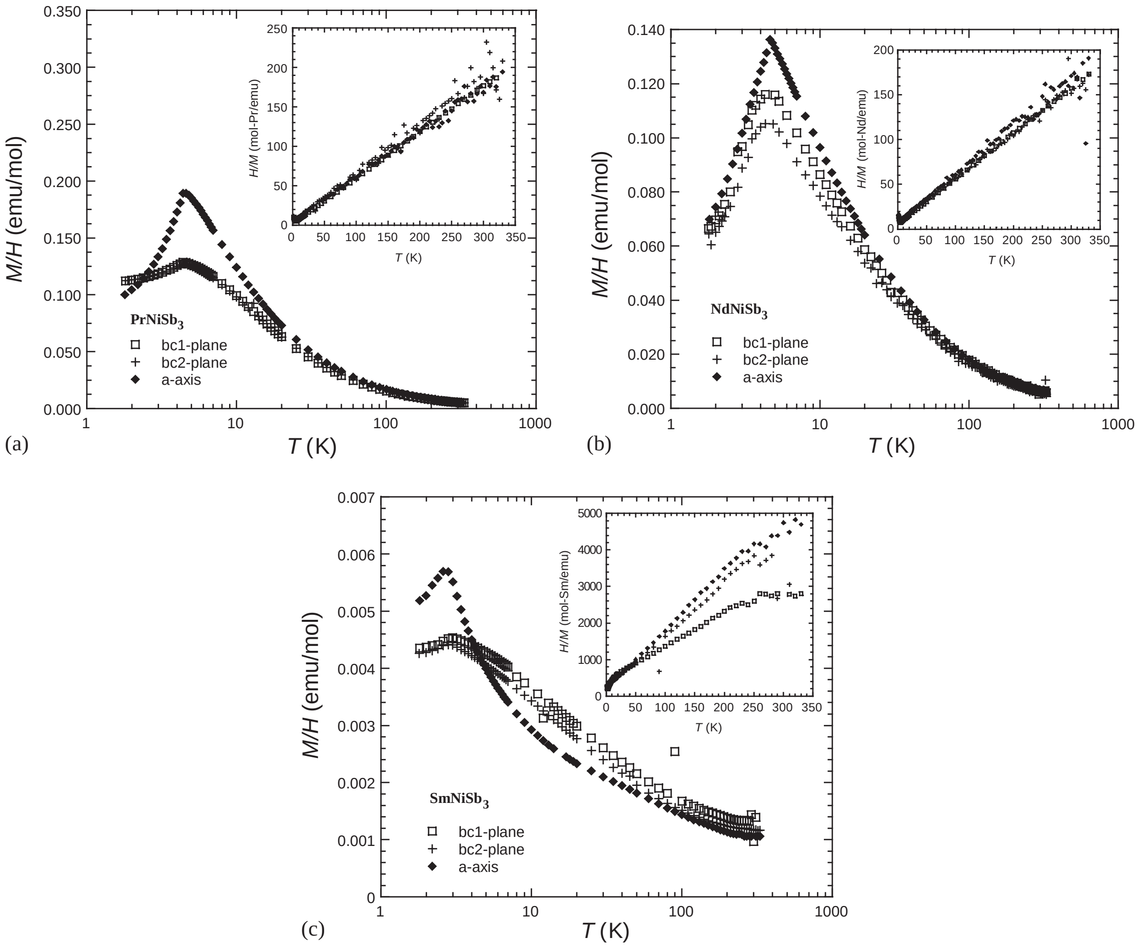

Fig. 2. Zero field-cooled magnetic susceptibility (M/H) as a function of temperature (T) in a magnetic field of $H = 1000$ G for single crystals of (a) $PrNiSb_3$ with $T_N = 4.5$ K, (b) $NdNiSb_3$ with $T_N = 4.6$ K, and (c) $SmNiSb_3$ with $T_N = 2.9$ K. Inset: inverse susceptibility with respect to temperature. The constant paramagnetic offset has been subtracted for $SmNiSb_3$.

Curie–Weiss fitting are 3.62 μ_B (PrNiSb$_3$), 3.90 μ_B (NdNiSb$_3$), and 0.80 μ_B (SmNiSb$_3$), which are in good agreement with those of Pr^{3+} (3.58), Nd^{3+} (3.62), and Sm^{3+} (0.84) as shown in Table 5. This along with the fact that LaNiSb$_3$ does not order magnetically down to 2 K indicates that the magnetic moments only come from the rare-earth atoms (Pr, Nd and Sm) and not Ni. Negative Weiss temperatures, θ_w, of ~ -5 K for PrNiSb$_3$, -10 K for NdNiSb$_3$, and $-10 \sim -40$ K for SmNiSb$_3$ suggest antiferromagnetic correlations.

Fig. 3 (a–c) shows magnetization data with respect to applied magnetic field. In PrNiSb$_3$ (Fig. 3a), the magnetization with the applied magnetic field oriented along the crystalline *a*-axis depends linearly on the field

Table 5
Magnetic properties of *Ln*NiSb$_3$ (*Ln* = Ce–Nd, Sm) compounds[a]

Compound	Ordering type	Ordering temperature T_C,* T_N (K)	μ_{Calc} [μ_B]	μ_{exp} [μ_B]	Reference
CeNiSb$_3$	FM	∼6.0*	2.54	∼2.54	[31]
PrNiSb$_3$	AFM	4.5	3.58	3.62	This work
NdNiSb$_3$	AFM	4.6	3.62	3.90	This work
SmNiSb$_3$	AFM	2.9	0.85	0.80	This work

[a] Abbreviations: FM, ferromagnetic; AFM, antiferromagnetic; μ_{exp}, experimental effective moment; μ_{Calc}, calculated effective moment for Ln^{3+}; T_C, Curie temperature; T_N, Néel temperature.

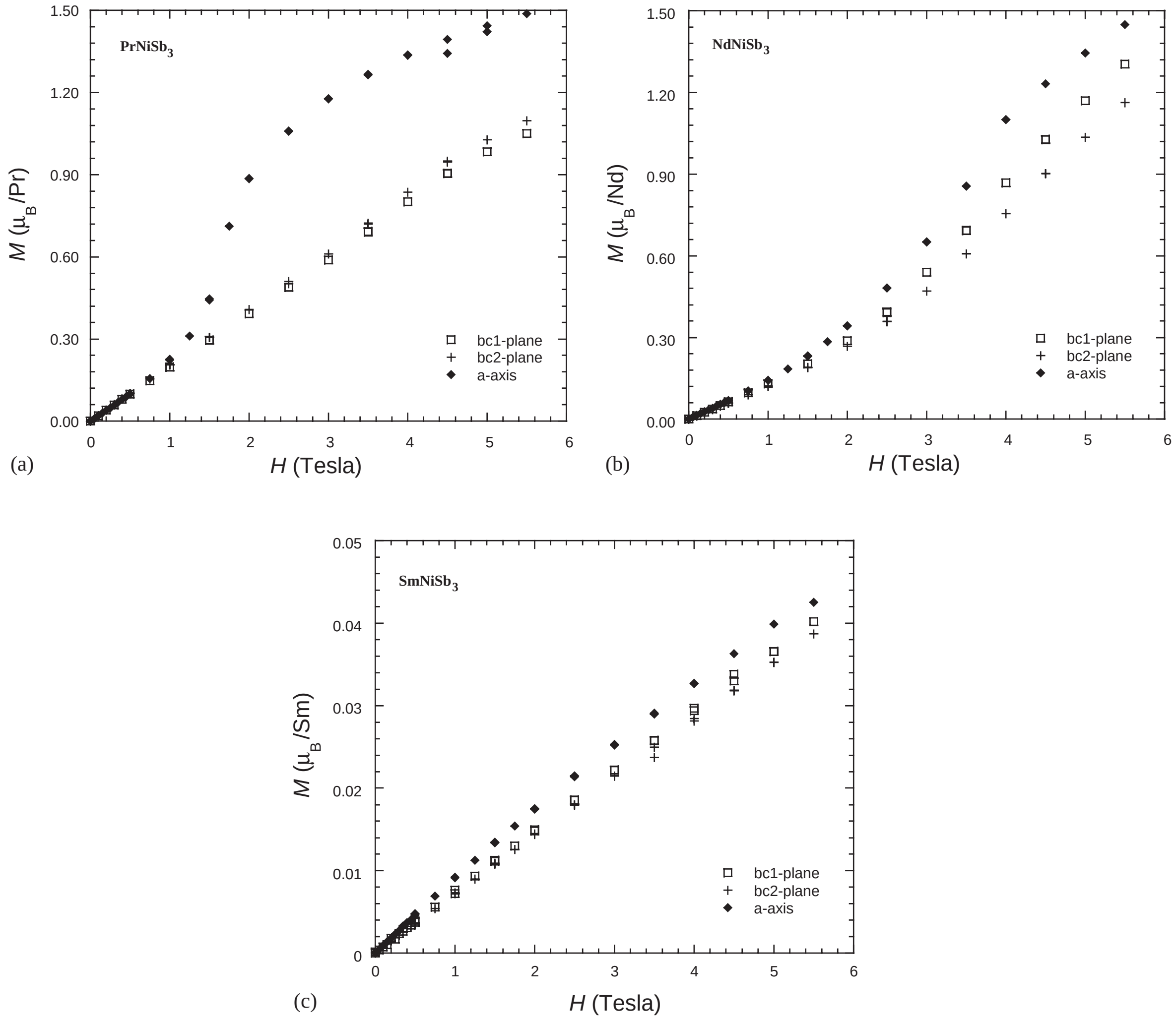

Fig. 3. Field-cooled magnetization (*M*) versus field (*H*) of (a) PrNiSb$_3$, (b) NdNiSb$_3$, and (c) SmNiSb$_3$ single crystals along the *bc*1- and *bc*2-planes and the *a*-axis at $T = 2$ K.

up to about 1 T. Above 1 T, it deviates from the linearity and increases rapidly up to 2 T. The slope is reduced again above 2 T. Similar behavior appears also in $NdNiSb_3$ (Fig. 3b) over a broader magnetic field range. This is most likely due to a spin–flop type of transition by an alternation of the spin arrangement, where antiferromagnetic alignment is broken partially under applied magnetic field. No magnetic-field-induced transition appears until 5.5 T in $SmNiSb_3$ (Fig. 3c), which shows relatively stronger antiferromagnetic correlation than the Pr and Nd cases, that is consistent with larger magnitude of the Weiss temperature.

The temperature dependence of the electrical resistivity of $PrNiSb_3$, $NdNiSb_3$ and $SmNiSb_3$ along the *bc*-plane is shown in Fig. 4. These compounds show metallic behavior with kinks at their Néel temperatures, indicating magnetic transitions. There are dramatic drops of the resistivity below the Néel temperatures due to antiferromagnetic ordering in $PrNiSb_3$ and $SmNiSb_3$. In $NdNiSb_3$, on the other hand, resistivity starts increasing suddenly below T_N. Similar features have been reported in Cr and URu_2Si_2 [28–30], where the enhancement of resistivity is attributed to partial gapping of the Fermi surface by the magnetic order.

3.3. Summary

The compounds, $PrNiSb_3$, $NdNiSb_3$, and $SmNiSb_3$ have been characterized by single crystal X-ray diffraction experiments. All three compounds are isostructural to $CeNiSb_3$ and are built up of Ln^{3+} atoms interleaved between layers of highly distorted, Ni-centered octahedra, and layers of buckled, nearly square Sb nets. The Sb sheets and Ni-centered octahedra in $SmNiSb_3$ contain the highest degree of distortion. The *Ln*–Sb distances are shortened for *Ln* = Ce–Sm, as expected. These *Ln*–Sb distances may play an important role in affecting the property measurements and RKKY interactions. $PrNiSb_3$, $NdNiSb_3$, and $SmNiSb_3$ are antiferromagnets with effective moments close to what is expected for Ln^{3+}. It is notable that all three phases have antiferromagnetically ordered ground states with low Néel temperatures, while a ferromagnetic state appears in the Ce analog. Moreover, the magnetic properties in Pr and

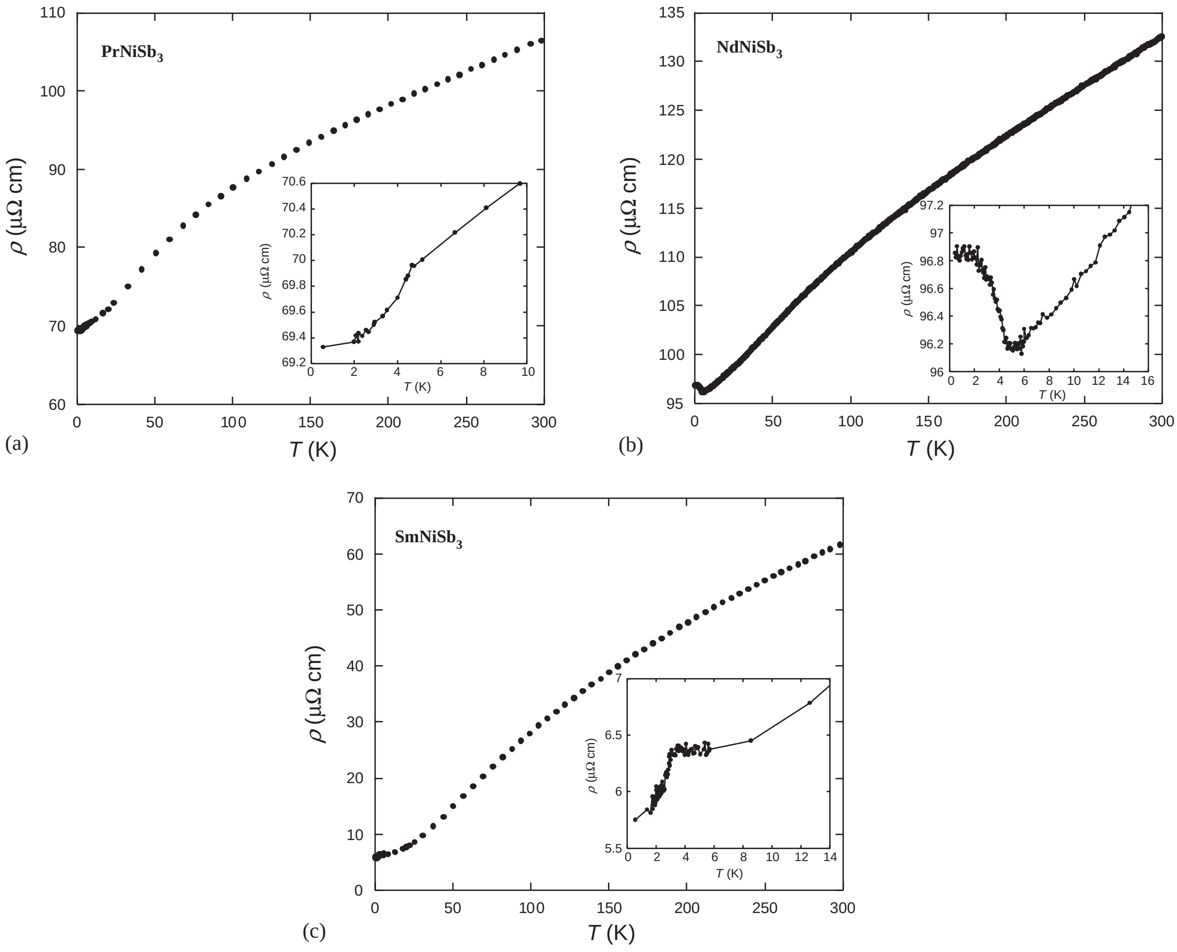

Fig. 4. Electrical resistivity of (a) $PrNiSb_3$, (b) $NdNiSb_3$, and (c) $SmNiSb_3$ between 0.5 and 300 K along the *bc*-plane. Insets: Low-temperature part of resistivity curve.

Nd are similar in that they have nearly the same Néel temperature and exhibit instability in their antiferromagnetic behavior under magnetic field above 1 T. The antiferromagnetic state in $SmNiSb_3$ is more stable in applied field than Pr and Nd.

It is worthwhile to note that $CeNiSb_3$ ($T_C \sim 6$ K) [31] is least distorted and has the highest ordering temperature of all the *Ln* analogs in this structure type. Examining the Pr-, Nd- and Sm-analogs, we have found that the octahedra in $SmNiSb_3$ are most distorted. This distortion may be significant in not only the stability of the structure type, but also the exchange interactions that may influence the ordering temperatures.

Acknowledgments

J.Y.C. acknowledges the PRF-G, NSF Career (DMR 0237664) and Alfred P. Sloan Fellowship for partial support of this project. Z.F. acknowledges NSF for partial support of this project.

References

[1] O. Sologub, P.S. Salamakha, in: K.A. Gschneidner, J.-C.G. Bünzli, V.K. Pecharsky (Eds.)., Handbook on the Physics and Chemistry of Rare Earths, vol. 33, Elsevier, Netherlands, 2003, p. 35.

[2] J.Y. Chan, S.M. Kauzlarich, P. Klavins, R.N. Shelton, D.J. Webb, Chem. Mater. 9 (1997) 3132.

[3] E.D. Bauer, N.A. Frederick, P.C. Ho, V.S. Zapf, M.B. Maple, Phys. Rev. B 65 (2002) 100506(R).

[4] A. Thamizhavel, T. Takeuchi, T. Okubo, M. Yamada, R. Asai, S. Kirita, A. Galatanu, E. Yamamoto, T. Ebihara, Y. Inada, R. Settai, Y. Onuki, Phys. Rev. B 68 (2003) 054427.

[5] M.J. Ferguson, R.W. Hushagen, A. Mar, J. Alloys Compd. 249 (1997) 191.

[6] D.D. Jackson, M. Torelli, Z. Fisk, Phys. Rev. B 65 (2002) 014421.

[7] M. Brylak, W. Jeitschko, Z. Naturforsch. 50b (1995) 899.

[8] K. Hartjes, W. Jeitschko, M. Brylak, J. Magn. Magn. Mater. 173 (1997) 109.

[9] N.P. Raju, J.E. Greedan, M.J. Ferguson, A. Mar, Chem. Mater. 10 (1998) 3630.

[10] E. Granado, H. Martinho, M.S. Sercheli, P.G. Pagliuso, D.D. Jackson, M. Torelli, J.W. Lynn, C. Rettori, Z. Fisk, S.B. Oseroff, Phys. Rev. Lett. 89 (2002) 107204.

[11] D.D. Jackson, Z. Fisk, J. Magn. Magn. Mater. 256 (2003) 106.

[12] L. Deakin, A. Mar, Chem. Mater. 15 (2003) 3343.

[13] L. Deakin, M.J. Ferguson, A. Mar, J.E. Greedan, A.S. Wills, Chem. Mater. 13 (2001) 1407.

[14] R.T. Macaluso, D.M. Wells, R.E. Sykora, T.E. Albrecht-Schmitt, A. Mar, S. Nakatsuji, H. Lee, Z. Fisk, J.Y. Chan, J. Solid State Chem. 177 (2004) 293.

[15] G.M. Sheldrick, SHELXL97, Program for Refinement of Crystal Structures, University of Göttingen, Germany, 1997.

[16] M. Brylak, M.H. Möller, W. Jeitschko, J. Solid State Chem. 115 (1995) 305.

[17] G. Cordier, H. Schafer, P. Woll, Z. Naturforsch. 40b (1985) 1097.

[18] A. Leithe-Jasper, P. Rogl, J. Alloys Compd. 203 (1994) 133.

[19] O. Sologub, K. Hiebl, P. Rogl, H. Noël, O.I. Bodak, J. Alloys Compd. 210 (1994) 153.

[20] O. Sologub, H. Noël, A. Leithe-Jasper, P. Rogl, O.I. Bodak, J. Solid State Chem. 115 (1995) 441.

[21] O. Sologub, K. Hiebl, P. Rogl, O.I. Bodak, J. Alloys Compd. 227 (1995) 40.

[22] P. Wollesen, W. Jeitschko, M. Brylak, L. Dietrich, J. Alloys Compd. 245 (1996) L5.

[23] H. Flandorfer, O. Sologub, C. Godart, K. Hiebl, A. Leithe-Jasper, P. Rogl, H. Noël, Solid State Commun. 97 (1996) 561.

[24] M.J. Ferguson, R.E. Ellenwood, A. Mar, Inorg. Chem. 38 (1999) 4503.

[25] R. Wang, H. Steinfink, Inorg. Chem. 6 (1967) 1685.

[26] Y.V. Pankevich, V.K. Pecharsky, O.I. Bodak, Russ. Metall. (1983) 189.

[27] T. Chen, J.C. Mikkelsen, G.B. Charlan, J. Crystal Growth 43 (1978) 5.

[28] E. Fawcett, H.L. Alberts, V.Y. Galkin, D.R. Noakes, J.V. Yakhmi, Rev. Mod. Phys. 66 (1994) 25.

[29] G.T. Meaden, K.V. Rao, K.T. Tee, Phys. Rev. Lett. 25 (1970) 359.

[30] T.T.M. Palstra, A.A. Menovsky, J.A. Mydosh, Phys. Rev. B 33 (1986) 6527.

[31] W. Bao, R.T. Macaluso, H.O. Lee, S. Nakatsuji, Z. Fisk, J.Y. Chan, in preparation.